



PAPER • OPEN ACCESS

Analysis of a high-stability Stern–Gerlach spatial fringe interferometer

To cite this article: Yair Margalit *et al* 2019 *New J. Phys.* **21** 073040

View the [article online](#) for updates and enhancements.

You may also like

- [A full quantum analysis of the Stern–Gerlach experiment using the evolution operator method: analyzing current issues in teaching quantum mechanics](#)
E Benítez Rodríguez, L M Arévalo Aguilar and E Piceno Martínez
- [High-Fidelity Manipulation of the Quantized Motion of a Single Atom via Stern–Gerlach Splitting](#)
Kun-Peng Wang, , Jun Zhuang et al.
- [Violation of Heisenberg's error-disturbance relation by Stern-Gerlach measurements](#)
Yuki Inoue and Masanao Ozawa



PAPER

OPEN ACCESS

RECEIVED
15 April 2019REVISED
10 June 2019ACCEPTED FOR PUBLICATION
8 July 2019PUBLISHED
23 July 2019

Original content from this work may be used under the terms of the [Creative Commons Attribution 3.0 licence](#).

Any further distribution of this work must maintain attribution to the author(s) and the title of the work, journal citation and DOI.



Analysis of a high-stability Stern–Gerlach spatial fringe interferometer

Yair Margalit¹ , Zhifan Zhou, Shimon Machluf, Yonathan Japha, Samuel Moukouri and Ron Folman

Department of Physics, Ben-Gurion University of the Negev, Be'er Sheva 84105, Israel

¹ Current address: Research Laboratory of Electronics, MIT-Harvard Center for Ultracold Atoms, Department of Physics, Massachusetts Institute of Technology, Cambridge, MA 02139, United States of America.E-mail: margalya@bgu.ac.il**Keywords:** matter-wave interferometry, Stern–Gerlach effect, atom chips

Abstract

The discovery of the Stern–Gerlach (SG) effect almost a century ago was followed by suggestions to use the effect as a basis for matter-wave interferometry. However, the coherence of splitting particles with spin by a magnetic gradient to a distance exceeding the position uncertainty in each of the arms was not demonstrated until recently, where spatial interference fringes were observed in a proof-of-principle experiment. Here we present and analyze the performance of an improved high-stability SG spatial fringe interferometer based on two spatially separate wave packets with a maximal distance that is more than an order of magnitude larger than their minimal widths. The improved performance is enabled by accurate magnetic field gradient pulses, originating from a novel atom chip configuration, which ensures high stability of the interferometer operation. We analyze the achieved stability using several models, discuss sources of noise, and detail interferometer optimization procedures. We also present a simple analytical phase-space description of the interferometer sequence that demonstrates quantitatively the complete separation of the superposed wave packets².

1. Introduction

The discovery of the Stern–Gerlach (SG) effect [1, 2] was followed by ideas concerning the construction of an SG interferometer (SGI), consisting of a freely propagating atom exposed to four magnetic gradients from macroscopic magnets [3]. The signal of this transverse closed-loop interferometer (i.e. with an enclosed area) is spin orientation at the output port, which is determined by the relative phase between the two spin components that propagate through the two arms. However, starting with Heisenberg, Bohm and Wigner [4] a coherent SGI was considered impractical because it was thought that the macroscopic device could not be precise enough to ensure a reversible splitting process. Englert, Schwinger and Scully analyzed the effect in more detail and named it the Humpty-Dumpty effect [5–7].

Attempts towards the implementation of an SGI as envisioned in the past were followed by impressive experiments where signals of spin coherence were detected in a longitudinal interferometer from a beam of atoms passing through regions with magnetic gradients [8–19]. These experiments suffered from three major drawbacks: first, there was no recombination stage and so the splitting could only be done to a distance on the order of the nano-meter scale coherence length, or else the signal was completely suppressed. Second, as this was a beam experiment, there was no possibility to analyze the results on an event-by-event basis, and third, there was no possibility to image the two wave packets to directly estimate their relative velocity and distance. Coherent splitting of an atomic cloud by the SG effect, where each atom is split into a superposition of spatially separated wave packets with a distance exceeding the position uncertainty in each of the arms, was demonstrated only recently in a proof-of-principle experiment [20]. The experiment used a recombination scheme based on the time-of-flight (TOF) expansion of the wave packets, after both wave packets were transformed into an

² We dedicate this work to mark the 100 year anniversary of the start of the Stern–Gerlach experiment in Frankfurt.

indistinguishable spin state. This was made possible by the long experimental times available due to the slow velocity of the atoms, initially trapped and prepared in a Bose–Einstein condensation (BEC) state, as well as the inherent nonlinearity of the applied magnetic gradients giving rise to a focusing (lensing) effect. Due to the large splitting (relative to the wave packet width), spatial interference fringes could be observed from the SG effect for the first time, turning this experiment into an analog of the double-slit experiment.

The interferometric scheme based on spatial interference fringes has an advantage over the closed-loop four-magnetic-gradients interferometer originally envisioned, in that it does not require very accurate recombination of two wave packets with different spins, as we demonstrate in this paper. Specifically, it is insensitive to imperfections of the wave packet shape, and to magnetic gradient imperfections giving rise to the Humpty-Dumpty effect. On the other hand, it requires high resolution imaging of the fringe patterns and therefore limits the final separations in position or momentum between the two wave packets. This limitation can be overcome by additional accelerating and stopping stages, as demonstrated with Bragg splitting [21]. Such robustness may eventually lead to advantageous technological applications.

Here we present an analysis of the performance of a high stability SG spatial fringe longitudinal interferometer, based on an atom chip [22], over a range of momentum splitting and separation distances allowed by the resolution of our imaging system (up to a differential velocity of $\sim 10 \text{ mm s}^{-1}$ after splitting and separation of $\sim 4 \text{ }\mu\text{m}$). For this range we show a multi-shot visibility (a measure of stability) larger than 90%, corresponding to a phase instability smaller than 0.45 radians. We analyze the sources of instability and compare to theoretical models. In addition, we present a quantitative description of the interferometric sequence in terms of relative phase-space coordinates (position and momentum). Using this description we show that before expansion and overlap the wave packets in the two interferometer arms are separated from each other by a distance of more than an order of magnitude larger than their width, which proves a full separation of the two interferometer arms.

The improved phase stability analyzed here was already used to realize a self-interfering atomic quantum clock [23], and to demonstrate a complementarity relation for such a clock interferometer [24].

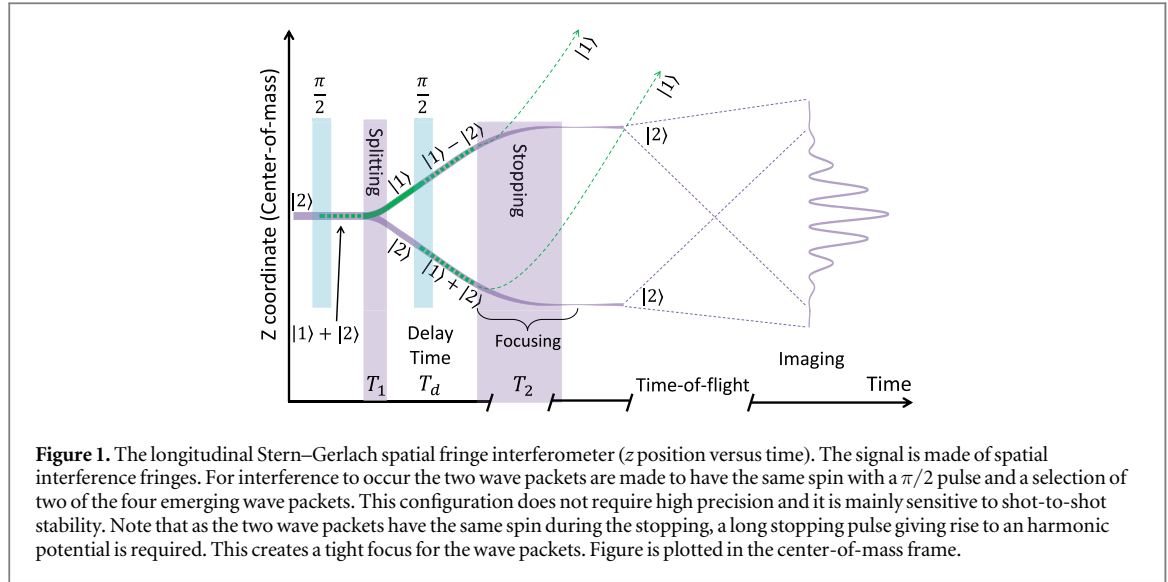
The structure of this paper is as follows. In section 2, we describe the experimental procedure and define our observable. In section 3 we present the achieved stability of the interferometric signal and compare it to theoretical models, discuss sources of instability, and detail the optimization procedure that enabled the high stability performance. In section 4 we present a phase-space description of the interferometric sequence and in section 5 we conclude and discuss possible future developments.

2. Interferometer sequence and signal

2.1. Experimental procedure

In our spatial fringe interferometer the initial atomic cloud is first prepared in a superposition of two spin states, which allows for splitting into two wave packets with different momenta using the SG effect, utilizing a pulsed magnetic gradient generated by the chip. The two wave packets split in space during free propagation, and are then rotated to have the same internal state. A second magnetic gradient pulse then stops the wave packets with respect to each other at a certain relative distance between them. After expansion and overlap of the wave packets spatial interference takes place, in a way that is analogous to a double-slit experiment with light. This sequence is different from a full-loop SGI [25, 26], where the two arms are kept with different spins throughout the sequence and recombined in space to form a spin population signal.

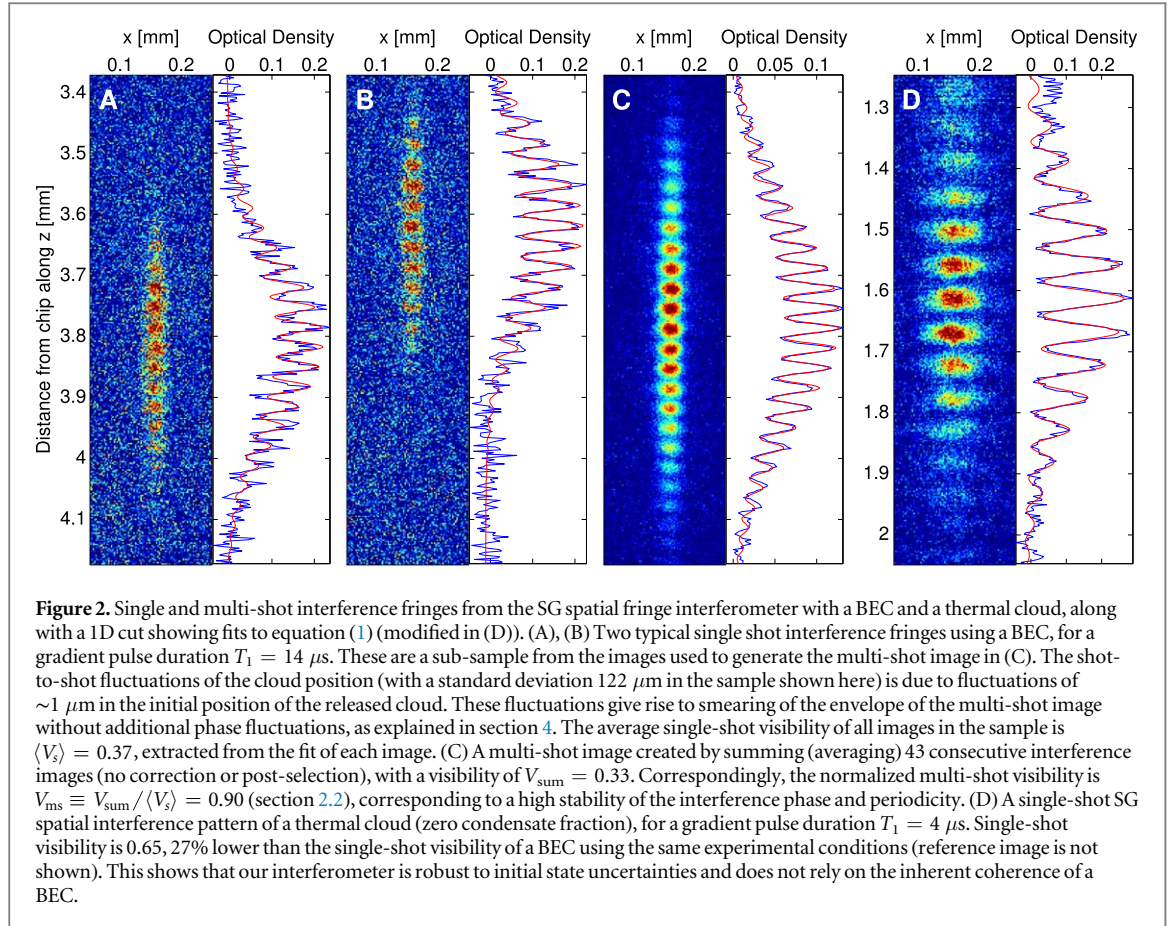
The experimental sequence is shown in figure 1. We begin by preparing a BEC of about 10^4 ^{87}Rb atoms in the state $|F, m_F\rangle = |2, 2\rangle$ in a magnetic trap located about $90 \text{ }\mu\text{m}$ below the surface of an atom chip, where the chip extends along the x - y plane at $z = 0$. The harmonic trap frequencies are $\omega_x/2\pi \approx 40 \text{ Hz}$ and $\omega_y/2\pi \approx \omega_z/2\pi \approx 126 \text{ Hz}$ where the BEC has a calculated Thomas–Fermi half-length of $\sim 9 \text{ }\mu\text{m}$ along x and $\sim 3 \text{ }\mu\text{m}$ along y and z . The trap is created by a copper structure located behind the chip with the help of additional homogeneous bias magnetic fields in the x , y and z directions (x is the direction of current on the chip, y the imaging axis, z the direction of gravity). The BEC is then released from the trap, and falls a few μm under gravity for a duration of 0.9 ms. During this time the magnetic fields used to generate the trap are turned off completely. Only a homogeneous magnetic bias field of 36.7 G in the y direction is kept on to create an effective two-level system via the nonlinear Zeeman effect such that the energy splitting between our two levels $|2, 2\rangle \equiv |2\rangle$ and $|2, 1\rangle \equiv |1\rangle$ is $E_{21} \approx h \times 25 \text{ MHz}$, and where the undesired transition to the $|2, 0\rangle$ state is off-resonance by $E_{21} - E_{10} \approx h \times 180 \text{ kHz}$. As the interferometer sequence is performed under conditions of free expansion, the time scale for many-body effects of atom-atom interaction are much longer than the duration of the sequence, so that the experiment may be described by single-atom physics (except for a mean-field repulsive potential that determines the initial shape and expansion rate of the BEC cloud).



Each atom in the atomic cloud is initially prepared in state $|2\rangle$. The interferometer sequence begins by applying a radio-frequency (RF) $\pi/2$ pulse (10 μs duration) to create an equal superposition of the two spin states, $|1\rangle$ and $|2\rangle$. A magnetic gradient pulse (splitting pulse) of duration $T_1 = 4\text{--}16\ \mu\text{s}$ creates a different magnetic potential $V_{m_j}(z)$ for the different spin states m_j , thus splitting the atomic spatial state into two wave packets with different momentum. The gradient pulse is generated by running current on the atom chip wires (see section 3.4 for details on the chip structure). Just after the splitting pulse, another RF $\pi/2$ pulse (10 μs duration) is applied creating a wave function made of four wave packets (similar to the beam splitter described in [20]): $|\mathbf{p}_\pm\rangle \equiv \frac{1}{\sqrt{2}}(|\mathbf{p}_1, \mathbf{x}_0\rangle \pm |\mathbf{p}_2, \mathbf{x}_0\rangle)$, where $|\mathbf{p}, \mathbf{x}\rangle$ represents a wave packet with momentum $\mathbf{p}_{1,2}$ acquired by states $|1\rangle$ and $|2\rangle$ during the splitting, and central position \mathbf{x} (\mathbf{x}_0 is the position of the atoms during the splitting pulse), and the plus and minus signs correspond to the final spin states $|1\rangle$ and $|2\rangle$, respectively (see figure 1). In this experiment we choose to work with the momentum superposition of the wave packets having spin $|2\rangle$ (while disregarding the superposition of $|1\rangle$, which after a second gradient (noted below) and TOF is at a different final position). The time interval between the two RF pulses (in which there are only two wave packets, each having a different spin) is reduced to a minimum ($\sim 40\ \mu\text{s}$) to suppress the hindering effect of a noisy and uncontrolled magnetic environment so that the experiment does not require magnetic shielding (see section 3.4 for more details). The minimal time between the two RF pulses is determined by a magnetic ‘tail’ of the gradient pulse, which at shorter times affects the resonance of the two-level system. A second magnetic gradient pulse of duration T_2 is designed to stop the relative motion of the two state $|2\rangle$ wave packets. As both wave packets have the same spin state, the magnetic gradient can stop their relative motion due to its curvature, as the slower wave packet is closer to the chip and hence experiences a stronger accelerating force relative to the faster wave packet which is further away. After this second pulse, the atoms fall under gravity. We then take an absorption image of the atoms and produce an optical-density image, as shown in figure 2.

In contrast to a full-loop SGI based on splitting and recombination of two wave packets with different spin states [25, 26], the spatial fringe interferometer provides an interference signal even if the recombination (stopping) is not precise, as long as the momentum distribution of each of the wave packets is wider than the momentum difference after stopping. It follows that this interferometer does not require high precision of the splitting and stopping operations but rather requires a high repeatability of these operations from shot to shot, which is essential for high phase stability.

The RF $\pi/2$ pulses are generated by an SRS SG384 RF signal generator, and subsequently amplified by a Minicircuit ZHL-3A amplifier. We modulate the RF power using a Minicircuit ZYSWA-2-50DR RF switch. The RF radiation is transmitted through two copper wires located behind the chip. The chip wire current is driven using simple 12 V batteries connected in series, and is modulated using a home-made current shutter (IGBT switch). The shot-to-shot charge fluctuations are measured to be $\delta Q/Q = 0.36\%$, where Q is the total charge running through the chip in a single pulse. The total resistance of the three chip wires is $13.51\ \Omega$ when the chip temperature has stabilized after a few hours of running the system (see section 3.4 for further details about chip design).



2.2. Normalized multi-shot visibility

The visibility and phase of the acquired atomic fringe patterns are extracted from the absorption image by taking a cut along z at the center of the wave packet envelope, and averaging along the x dimension to reduce noise. The one-dimensional cut is then fitted to a sine function with a Gaussian envelope

$$n(z) = A \exp\left[-\frac{(z - z_0)^2}{2\sigma^2}\right] \times \left[1 + V \sin\left(\frac{2\pi}{\lambda}(z - z_{\text{ref}}) + \phi\right)\right] + c, \quad (1)$$

where the fitting parameters are the amplitude A , the center position z_0 , the Gaussian width σ , the fringe periodicity λ , the interference fringes visibility V , and the phase ϕ . z_{ref} is a fixed phase reference point (usually taken to be middle of the image). Typical fitting results can be seen in figure 2.

The visibility of single-shot images in our experiment can be quite high (~ 0.9 for certain experimental parameters), while the main effect of instability is shot-to-shot fluctuations of the phase. In order to characterize the stability of the phase, which is the main figure of merit in interferometry, we use as our signal the multi-shot image made by summing many interference patterns one on top of the other with no post-selection or alignment (each interference pattern is a result of one experimental cycle), and dividing by the number of patterns (such that the multi-shot is an average). Large phase noise and interference periodicity noise in a set of single-shot images would result in a low multi-shot visibility, while low noise corresponds to high multi-shot visibility (see section 3.3; a quantitative relation is derived in appendix A.2). The multi-shot visibility is therefore a measure of the stability of the phase and periodicity. As in the single-shot case, we extract the multi-shot visibility by fitting the multi-shot sum image to the form of equation (1) (see figure 2(C)).

In order to eliminate technical effects irrelevant to stability which affect the multi-shot visibility, we normalize the multi-shot visibility to the mean of the single-shot visibilities taken from the same sample. This normalization eliminates effects such as visibility reduction due to an impure BEC (thermal atoms), lack of perfect overlap between the wave packet envelopes in 3D, as well as imaging limitations such as inaccurate focal point, limited focal depth, spatial resolution, movement of the interference fringes relative to the camera during the image integration time (smearing), and so on. The normalized multi-shot visibility V_{ms} is therefore given by $V_{\text{ms}} \equiv V_{\text{sum}} / \langle V_s \rangle$, where V_{sum} is the (un-normalized) visibility of the multi-shot sum image extracted from the fit, and $\langle V_s \rangle$ is the mean visibility of the single-shot images which compose the multi-shot image. The error bars are estimated by

$$\Delta V_{\text{ms}} = V_{\text{ms}} \times \sqrt{\left(\frac{\Delta V_{\text{sum}}}{V_{\text{sum}}}\right)^2 + \frac{1}{N} \left(\frac{\Delta V_s}{\langle V_s \rangle}\right)^2 + \frac{1}{2N} \left(\frac{1 - V_{\text{ms}}^2}{V_{\text{ms}}}\right)^2}, \quad (2)$$

where ΔV_{sum} is the fit error of the visibility of the multi-shot sum image, ΔV_s is the measured standard deviation of the single-shot visibility (N being the sample size), and the third term under the square root estimates the expected relative standard error of the normalized multi-shot visibility due to the finite sample size (see appendix A.2 for the derivation).

The normalized multi-shot visibility reflects shot-to-shot phase fluctuations between the single fringe patterns in the sample. Phase fluctuations along the fringe axis include fluctuations of the global phase ϕ of the single-shot patterns (with standard deviation $\delta\phi$) and of the single-shot fringe periodicity $\lambda = 2\pi/\kappa$ (with standard deviation $\delta\kappa$ for the wave number κ). As shown in appendix A.2, these fluctuations are related to the multi-shot visibility by

$$V_{\text{ms}} \approx \exp\left[-\frac{1}{2}(\delta\phi^2 + \sigma_{\text{ms}}^2 \delta\kappa^2)\right], \quad (3)$$

where σ_{ms} is the Gaussian width of the multi-shot pattern. A more accurate theoretical expression for the multi-shot visibility and an alternative definition of V_{ms} based on a more general mathematical procedure rather than a fit is also given in section 3.3.

3. Stability analysis and optimization

In this section we present the optimal stability of the SG spatial fringe interferometer in terms of the normalized multi-shot visibility, which represents the stability of the interferometric phase, as defined above in section 2.2. This optimal stability has been achieved after an optimization procedure described below in section 3.4. In addition to measuring the optimal stability and in order to demonstrate the mechanism leading to phase instability we have also examined the effect of a specific source of instability—fluctuations of the splitting pulse strength—on the multi-shot visibility. The experimental results are compared to a few theoretical models described in section 3.3.

3.1. Optimal stability

Figure 3 shows the measured normalized multi-shot visibility, V_{ms} , as a function of the splitting gradient pulse duration. The upper data points (blue and magenta circles) represent the multi-shot visibility after optimizing the sequence, compared with predictions from several theoretical models (see section 3.3). We find high multi-shot visibility ($> 90\%$) for momentum splitting up to 10 mm s^{-1} , the equivalent of $\sim 2\hbar k$ (where $\lambda = 1 \text{ }\mu\text{m}$ as a reference comparing to laser pulse Raman interferometers), corresponding to a high stability of the phase and interference pattern periodicity. These results demonstrate the current stability limits of our interferometer.

In table 1 we present the parameters used for each data point in figure 3. The free propagation time T_d between the pulses and the stopping pulse duration T_2 were chosen so as to optimize the multi-shot visibility by minimizing the effect of fluctuations in parameters of the interferometric sequence such as the initial trapping position or the stopping pulse duration, as detailed in section 3.4.

In table 1 we also show some wave packet parameters calculated from the experimental parameters or by using equations (11), (12), and (16) in section 4. We compare the experimental and theoretical values of the wave packet separation, d , at the end of the stopping pulse. The experimental value of d is calculated by substituting the measured spatial period of the fringes λ into $d = \hbar T_f / m \lambda$, where T_f is the TOF (equation (16)). The theoretical value of the separation is calculated from equation (12) by using the experimental parameters, with an estimated value $\omega = 2\pi \times 800 \text{ Hz}$ for the stopping pulse curvature, averaged over the range spanned while the atoms move (see section 4). The theoretical result differs from the values calculated from the fringe periodicity by no more than 4%. The separation d is larger than the minimal Gaussian wave packet width σ_{min} by a factor 8–33. This minimum wave packet size is due to the focusing power of the stopping pulse, as discussed in section 4 and depicted in figure 1. The spatial separation being much larger than the minimum wave packet width is an experimental fact that is evident from the appearance of multiple fringes in the final interference pattern (d/σ_{min} roughly represents the number of interference fringes of a single pattern). However, this wave packet separation is inversely proportional to the spatial period of the fringes, λ , and as our TOF is experimentally limited by the field of view of the camera and its sensitivity, it follows that the wave packet separation is limited by the practical resolution of the imaging system and cannot exceed the maximal value of about $4 \text{ }\mu\text{m}$. Such a separation corresponds to a fringe periodicity of about $25 \text{ }\mu\text{m}$ for the used values of TOF (as our optical resolution is $\sim 5 \text{ }\mu\text{m}$, and it is necessary to measure several points in order to distinguish a fringe pattern). Such a fringe pattern was observed in our experiment (magenta point in the optimal stability data in figure 3). Another effect limiting the observation of small-periodicity interference patterns is smearing of the

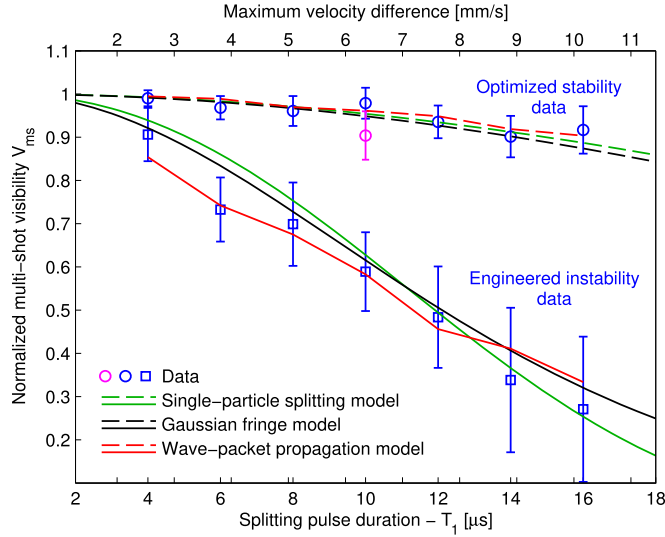


Figure 3. Analysis of interferometer stability: normalized multi-shot visibility (a measure of stability) versus splitting pulse duration T_1 . Data show the multi-shot visibility of sequences that minimize phase fluctuations (optimized stability—blue and magenta circles), and similar sequences where current fluctuations were artificially injected into the splitting pulse in order to examine the effect of instability (engineered instability—blue squares). The optimized stability data demonstrates the high stability achieved in the experiment (the magenta point corresponds to the largest obtained wave packet separation of $4 \mu\text{m}$). Dashed and solid lines show predictions of several theoretical models (see section 3.3 for a description). The timings are detailed in table 1. The raw data for the $T_1 = 14 \mu\text{s}$ optimized stability data point is shown in figure 2. Error bars include fitting errors for each multi-shot pattern, standard error of the mean (SEM) of single-shot visibility, and uncertainty due to the finite sample size (equation (2)), and do not account for long term drifts.

Table 1. Parameters of the interferometer data points in figure 3: T_1 , T_d , T_2 , and TOF are time durations of stages of the interferometer sequence (as defined in figure 1). $\langle V_s \rangle$ is the mean single-shot visibility for each data set. The separation d achieved during the sequence is calculated from the experiment using the observed periodicity of the interference pattern λ (equation (16)), and theoretically by the analytic equation (12), using the experimental parameters, with an estimated effective harmonic frequency of $\omega/2\pi = 800 \text{ Hz}$. The scaling factor ξ describes the squeezing in phase space (see section 4, equation (11)), and σ_{\min} describes the minimal wave packet width at the focal point (equation (15)). Note that the initial wave packet width is $\sigma_{z,0} = 1.2 \mu\text{m}$ [25]. The last column describes the parameters of the large wave packet separation sequence (magenta data point in figure 3). Same parameters were used for both the optimized stability and the engineered instability data (except for the last column, used only in the optimized stability case).

$T_1 (\mu\text{s})$	4	6	8	10	12	14	16	10
$T_d (\mu\text{s})$	116	174	132	90	130	106	114	600
$T_2 (\mu\text{s})$	200	150	180	220	200	200	200	70
TOF (μs)	6760	6750	8760	12 760	12 738	13 810	13 800	21 450
$\langle V_s \rangle$	0.75	0.52	0.44	0.42	0.45	0.37	0.29	0.34
No. images	40	45	42	64	41	43	47	45
exp. $d (\mu\text{m})$	0.55	0.98	1.14	1.31	1.66	1.92	2.25	3.93
theo. $d (\mu\text{m})$	0.57	0.99	1.19	1.37	1.79	1.94	2.21	3.90
Scaling factor ξ	1.16	1.34	1.21	1.11	1.21	1.13	1.12	3.36
$\sigma_{\min} (\text{nm})$	68	79	71	65	71	66	66	190

pattern due its movement during CCD integration (imaging), an effect which increases as the periodicity decreases. This effect combined with the limited optical resolution causes the single-shot visibility $\langle V_s \rangle$ to decrease as the periodicity decreases (d increases), as seen in table 1.

In figure 4 we demonstrate the achieved stability after the optimization procedure, by showing the interferometer phase stability over more than 3 h of continuous data taking. Although the experimental parameters are the same as those used for the data point of $T_1 = 10 \mu\text{s}$ in figure 3, the multi-shot visibility for this data set reduced to $V_{\text{ms}} = 0.89$. We attribute this reduction to the fact that the data in figure 4 were taken a few weeks after the optimization procedure leading to the stability of the data set used for figure 3, such that during this time long time drifts have driven the system away from the optimal stability parameters.

The shot-to-shot fluctuations leading to the reduction of visibility in the optimized interferometer sequence follow mainly from fluctuations in the interferometer device (i.e. gradient pulse durations and currents) and not from fluctuations of the initial BEC preparation. This is further demonstrated in figure 2(d), where we show a

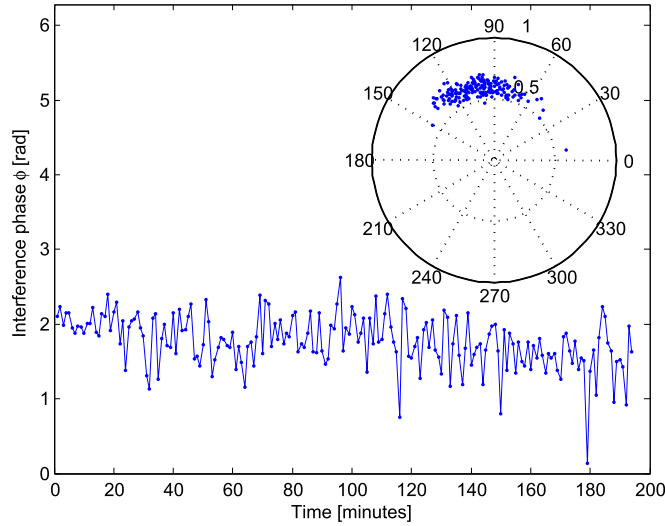


Figure 4. Interferometer phase stability over a few hours: phase as a function of time, for $T_1 = 10 \mu\text{s}$, $T_d = 90 \mu\text{s}$, and $T_2 = 220 \mu\text{s}$. The standard deviation of the phase is 0.37 rad, and the normalized multi-shot visibility is $V_{\text{ms}} = 0.89 \pm 0.03$. Evaluating equation (3) with the experimental parameters $\delta k = 2\pi \cdot \delta\lambda/\lambda^2 = 2636 \text{ [1/m]}$ and $\sigma_{\text{ms}} = 170 \mu\text{m}$, we obtain $V_{\text{ms}} = 0.851$. The small discrepancy between the experimental and theoretical values is probably due to correlations between center position and the periodicity and phase (see appendix A.2 for discussion). Inset: a polar plot of phase versus single-shot visibility (shown as angle versus radius).

single-shot SG spatial interference pattern of a thermal cloud (zero condensate fraction), instead of a BEC. The high single-shot visibility proves that our interferometer is robust to initial state uncertainties and does not rely on the inherent coherence of a BEC. Since a thermal cloud has a larger initial size (compared to a BEC), each part of the cloud feels a different force due to the inhomogeneous gradient (nonlinear magnetic field pulse), causing a wavelength chirp of the resulting interference fringes. To account for this effect, we fit image figure 2(d) by modifying the argument of the sine function in equation (1) to $\phi + \frac{2\pi}{\lambda}(z - z_{\text{ref}}) + k_1(z - z_{\text{ref}})^2$, where the parameter k_1 represents the wavelength chirp.

3.2. Engineered instability

Let us now examine the effect of a single source of instability, namely, fluctuations of the chip current during the splitting of the atoms, on the instability of the interferometric phase and its consequent effect on the normalized multi-shot visibility. In order to demonstrate this effect we have engineered artificial fluctuations of the current and examined the resultant suppression of the multi-shot visibility. The engineered instability data is presented in figure 3 (blue squares).

The engineered instability data was produced by changing the chip voltage driving the splitting pulse using a voltage stabilizer circuit, with corresponding variable values of chip current, and recording several experimental cycles for each value of the current. The stopping pulse current was kept constant. Figure 5 shows the resulting single shot interference phase as a function of the applied chip current during the first gradient pulse T_1 , where a clear linear relation to the applied chip current is seen. These data are used to produce the engineered instability data in figure 3.

The engineered instability multi-shot fringe patterns are produced by summing over the many single-shot images composing figure 5, with different values of the splitting pulse currents. In order to properly emulate the spectrum of natural noise, the averaged image is obtained by taking a weighted average of single-shot images such as to create a normal distribution of currents, where its width is set to $\delta I/I = 15.47 \text{ mA}/860 \text{ mA} = 1.8\%$. As the phase is linear with the applied current, such a distribution corresponds to a normal distribution of phases. Summing multiple phases and periodicities causes a chirp of the interference periodicity, and a spatial chirp of the interference visibility. Due to these chirping effects, we cannot extract the visibility of these multi-shot images by fitting the pattern to equation (1). See appendix A.1 for an explanation of the visibility extraction process.

Since the engineered instability data presented in figure 3 were taken a few months after taking the optimized stability data, the same experimental parameters gave normalized multi-shot visibility 2%–10% lower than the original data, due to long term drifts. To suppress the effect of this drift on the engineered instability data, we normalized each measurement to a corresponding one using the same experimental parameters, in which zero noise was added (i.e. the chip current was held constant throughout the measurement). Normalization is done

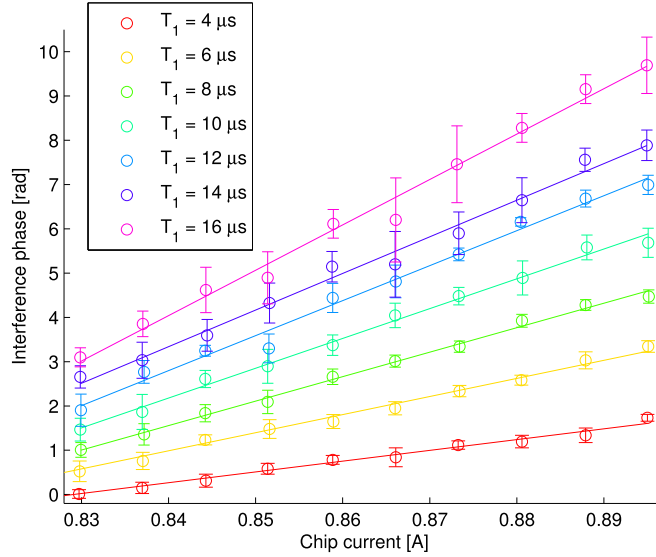


Figure 5. Interference phase as a function of the applied chip current during the first gradient pulse T_1 , used to produce the engineered instability data in figure 3. The phase data has been shifted vertically for clarity. The phase is clearly linear with the applied chip current, and we also confirm that the slope divided by T_1 of all curves is equal within error bars, as would be expected from theory. The mean slope divided by T_1 is $\partial\phi/\partial I_1/T_1 = 6.49 \text{ rad A}^{-1} \mu\text{s}^{-1}$.

by dividing V_{ms} of the engineered instability data by V_{ms} of the reference zero-added-noise data (taken within the same data set). The result of such a normalization is that only the injected noise affects the results.

One can see that the error bars of the engineered instability data in figure 3 are much bigger than those of the optimized stability data. We explain this by noting that the error bars are estimated using equation (2), in which the third term under the square root estimates the expected relative standard error of the normalized multi-shot visibility due to the finite sample size (equation (A13)), and is given by $(1 - V_{\text{ms}}^2)^2 / (2NV_{\text{ms}}^2)$. Since this factor grows larger as V_{ms} approaches low values, it results in a large error estimation, even when the number of single shots N is high ($N = 138$ – 267 for the engineered instability data).

3.3. Theoretical models

For generating the theoretical curves in figure 3 we have used numerical and analytical models. As can be seen, all models show good agreement with both optimized stability and engineered instability data sets.

The single-particle splitting model (dashed and solid green lines in figure 3, for the optimized stability and engineered instability runs, respectively) is a straight-forward numerical quantum simulation of a noisy single-particle splitting process similar to the splitting done in our experiment. The validity of this model is based on the fact that the stopping pulse is optimized for completely stopping the relative motion of the two wave packet centers, and that the major source of shot-to-shot fluctuations is in the splitting pulse of duration T_1 . In this case the interference fringe patterns observed after a long TOF are a scaled (magnified) copy of the interference patterns formed just after the splitting pulse as a result of the differential phase gradient imprinted on the initial wave-packets of the two spin states (equivalent to a differential momentum transfer), as shown in section 4. Therefore this model takes the multi-shot visibility of the fringes formed just after the splitting pulse as representing the visibility expected to be observed in the actual experiment. The relative fluctuations of the magnetic field amplitude during splitting are assumed to have a Gaussian distribution, with a standard deviation of $\delta B/B$ (for zero noise in the splitting pulse timing, this would be equal to $\delta I_1/I_1$, where I_1 is the current of the splitting pulse). The Schrödinger equations for the evolution of the two wave packets $\psi_1(z, t)$ and $\psi_2(z, t)$, corresponding to the two spin states, are solved many times for different values of $\delta B/B$ and the resulting interference patterns are summed up to yield a multi-shot pattern, which is then fitted to the form of equation (1) to extract the multi-shot visibility. The values used for $\delta B/B$ were 0.69% and 1.8%, respectively for the optimized stability and engineered instability data. The first value was chosen to produce a fair fit for the data, while the second is the experimental value used for $\delta I_1/I_1$ when producing the added noise. The agreement of this simplified model with the experimental results demonstrates the sensitivity of our interferometer to the fine details of the magnetic field and its fluctuations during the splitting.

The Gaussian fringe model (dashed and solid black lines in figure 3, for the optimized stability and engineered instability runs, respectively) is an analytical phenomenological model of fringe patterns assuming Gaussian fluctuations of three parameters characterizing the single-shot fringe patterns: phase ϕ , wave-number

$\kappa \equiv 2\pi/\lambda$ and center position z_0 (see equation (1)). The standard deviations of these parameters are correspondingly denoted by $\delta\phi$, $\delta\kappa$, and δz . In appendix A.2 we show that, regardless of the source of these fluctuations, such an assumption leads to the following form for the multi-shot visibility:

$$V_{\text{ms}} = \frac{\exp\left[-\frac{1}{2} \frac{\delta\phi^2}{1 + \sigma_{\text{ms}}^2 \delta\kappa^2}\right]}{\sqrt{1 + \sigma_{\text{ms}}^2 \delta\kappa^2}}, \quad (4)$$

where $\sigma_{\text{ms}} = \sqrt{\sigma^2 + \delta z^2}$ is the Gaussian width of the multi-shot fringe pattern, with σ being the width of the single-shot pattern as in equation (1). Although this model does not rely on the assumption of optimal stopping as in the previous model, the specific form of equation (4) is obtained for the case where the phase and wave-number fluctuations are correlated, which is true at least in the case of the engineered instability data, where the main source of fluctuations is current instability during the splitting pulse. Since the fringes observed after TOF are a scaled picture of the microscopic fringes created just after the splitting pulse (section 4), we may replace all the parameters in equation (4) with the corresponding parameters of the microscopic imprinted fringes, where $\delta\kappa$ is the wave-number fluctuation which is equal to the fluctuation of the differential momentum transfer $\hbar k$ ($k = 0.9 (\mu\text{m } \mu\text{s})^{-1} \times T_1(\mu\text{s})$, $\delta z = 1 \mu\text{m}$ corresponds to the initial trapping position fluctuations and $\sigma = 1.2 \mu\text{m}$ is the Gaussian width of the initial BEC cloud). The relation between these fluctuations is then $\delta\phi/\delta\kappa = z_i$, where z_i is the distance of the mean atomic cloud center from the magnetic field quadrupole center during the splitting pulse. The theoretical curve of the engineered instability data in figure 3 was calculated by using equation (4) assuming $z_i = 5 \mu\text{m}$, and using $\sigma_{\text{ms}} = 1.56 \mu\text{m}$ (wave-packet width + initial position uncertainty), and $\delta\kappa/\kappa = 1.8\%$ (value of the induced fluctuations). For the optimized visibility data, where V_{ms} is high, the correlation between the phase and wave-number fluctuations is not important, as the theoretical expression for V_{ms} can be approximated by equation (3) regardless of this correlation. In this case if we assume a relation between $\delta\kappa$ and $\delta\phi$ as above we need to take $\delta\kappa/\kappa = \delta\phi/\phi = 0.69\%$ in order to reproduce a fair fit to the data. This value for the fluctuations is about twice higher than the independently measured fluctuations of the current \times pulse duration $Q_1 = I_1 T_1$ of $\delta Q_1/Q_1 \approx 3.6 \times 10^{-3}$ in the splitting pulse. The discrepancy may be attributed to the fact that an important source of fluctuations is also the stopping pulse, whose contribution to the fluctuations is not known from this model.

The wave-packet propagation model (dashed and solid red lines in figure 3, for the optimized stability and engineered instability runs, respectively) uses a semi-analytical method in which the three-dimensional trajectory of each of the two wave-packet centers is calculated by solving Newton's equations of motion in the presence of magnetic forces and gravity along the whole interferometric sequence: from trap release to observation after TOF [27]. In the center-of-mass frame of each wave packet we derive the wave-packet evolution by taking a quadratic approximation for the magnetic atomic potential and solving for the scaling factors describing the wave-packet sizes along the three axes [28–30]. This allows to reconstruct the wave packets' shape at the measurement time and hence the shape of the interference fringes at each experimental realization. This method allows to introduce fluctuations of the current, timing or positions of the wave packets at any part of the interferometric sequence. In figure 6 we show a comparison between the results of this model and the experimental results for the final position and interference wavelength (periodicity λ). One can see that our numerical wave-packet propagation simulation estimates the basic parameters of the interferometer with an accuracy of 1%. For the optimized stability data the model assumes relative current fluctuations $\delta I_1/I_1 = \delta Q/Q = 0.36\%$ during the splitting pulse (using the independently measured value of the relative charge fluctuations $\delta Q/Q$), and $\delta I_2/I_2 = 0.05\%$, during the stopping pulse. As the fluctuations in the stopping pulse were not directly measured, we use a number that best fits the experimental data. The fact that the stopping pulse fluctuations are smaller may originate from the decreasing difficulty to generate stable long duration pulses relative to short duration pulses, e.g. since timing jitter becomes less dominant for longer pulses.

For the engineered instability data we show a theoretical curve calculated by using the induced fluctuations ($\delta I_1/I_1 = 1.8\%$) during the splitting pulse. The numerical visibility was normalized to the multi-shot visibility of simulated fringe patterns whose fluctuations are purely due to initial position fluctuations $\Delta z_{\text{initial}}$ of $1 \mu\text{m}$ (standard deviation) around $z = 87.5 \mu\text{m}$ from the chip.

3.4. Optimization and suppression of instability

A major source of phase noise for the interferometer are the shot-to-shot current fluctuations in the chip wires, which cause fluctuations of the magnetic field energy during the time between the two $\pi/2$ pulses, in which the two wave packets occupy two different spin states [20]. The previous realization of the interferometer used a single wire on the atom chip to generate the required magnetic gradients. This setup showed limited stability in the phase and periodicity of the resulting interference fringes [20].

To address this problem, we have designed and fabricated a new atom chip. In the new design, the magnetic gradient pulses are generated by three parallel gold wires (along x) located on the chip surface (see figure 7),

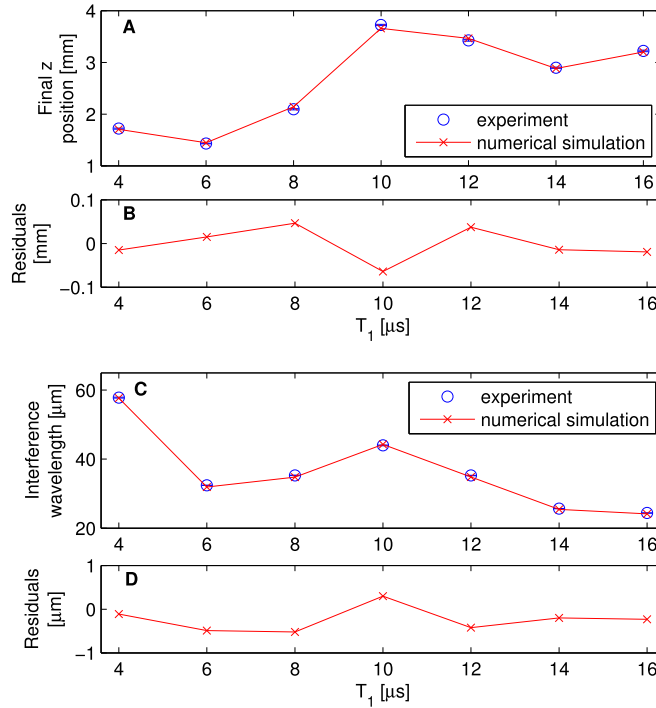


Figure 6. Comparison between the interferometer experimental results and the numerical wave-packet propagation model. (A) Final z position as a function of the first gradient pulse duration T_1 . (B) Residuals showing the difference between the experiment and the simulation in (A). The mean absolute residual is 1.15%. (C) Periodicity λ of the interference pattern as a function of the first gradient pulse duration T_1 . (D) Residuals showing the difference between the experiment and the simulation in (C). The mean absolute residual is 0.97%. The lines in (A) and (C) are not monotonic since these are different points in a multi-dimensional space: T_1 is not the only parameter that changes between each point, but also T_{db} , T_2 , and the time-of-flight, due to the complex optimization process. Lines are therefore only a guide to the eye. Experimental error bars represent standard error of the mean.

which are 10 mm long, 40 μm wide and 2 μm thick. The wires' centers are separated by 100 μm , and the same current runs through them in alternating directions, creating a 2D quadrupole field (in the yz plane) with its center at $z = 98 \mu\text{m}$ below the atom chip. The phase noise is largely proportional to the magnitude of the magnetic field responsible for the gradient [20], whereas the fluctuations in the stable current in the external coils giving rise to the homogeneous bias field (along y) are relatively small. As the main source of magnetic instability is in the gradient pulse originating from the chip currents, positioning the atoms near the middle (zero) of the quadrupole field created solely by the three chip wires 98 μm below the chip surface reduces the phase noise (see figure 7 for more details).

Let us note that as the durations of our interferometer operation and work-cycle are 100 μs (without TOF) and 60 s respectively, and as we take data for several hours in each run, we believe we are sensitive to fluctuations with frequencies lower than about 10 kHz. As the shortest magnetic gradient pulse is 4 μs , we may even be sensitive to frequencies up to 100 kHz. This captures the dominant part of the $1/f$ (flicker) noise of electronic systems.

In addition to the novel chip design, we have applied, as shown in figure 8, several optimization procedures which aim to minimize the hindering effects of fluctuations. First, in figure 8(a) we optimize the splitting position to be close to the quadrupole center, since this is where the magnitude of the field is smallest and consequently, as explained previously, the fluctuations are minimized. Let us elaborate. The initial trapping distance determines the position of the atoms relative to the magnetic quadrupole created by the chip wires during the gradient pulses. At a given distance $|z - z_{\text{quad}}|$ from the quadrupole center the differential phase fluctuations $\delta\phi$ are proportional to the relative current fluctuations, such that $\delta\phi = -\Delta m_F g_F \mu_B \delta B T_1 / \hbar = k |z - z_{\text{quad}}| (\delta I / I)$, where $k = \Delta m_F g_F \mu_B B' T_1 / \hbar$ is the differential momentum kick during the splitting pulse (B' being the magnetic field gradient), μ_B is the Bohr magneton and $\Delta m_F = 1$. Here we have assumed that the magnetic field fluctuations are proportional to the current fluctuations, $\delta B = B' |z - z_{\text{quad}}| (\delta B / B) = B' |z - z_{\text{quad}}| (\delta I / I)$. Although the phase fluctuations $\delta\phi$ at the average position of the center of the cloud during the splitting may vanish completely if the latter coincides with the quadrupole center, perfect visibility is not expected to be achieved due to the fluctuations of the field gradient itself and the finite size of the atomic cloud (6 μm edge to edge in the Thomas–Fermi approximation), and the shot-to-shot fluctuations of the initial trapping position (about $\pm 1 \mu\text{m}$), as can be seen from equations (3) and (4). In addition, visibility may also reduce due to imperfections in other stages of the interferometer sequence. Figure 8(a) shows the

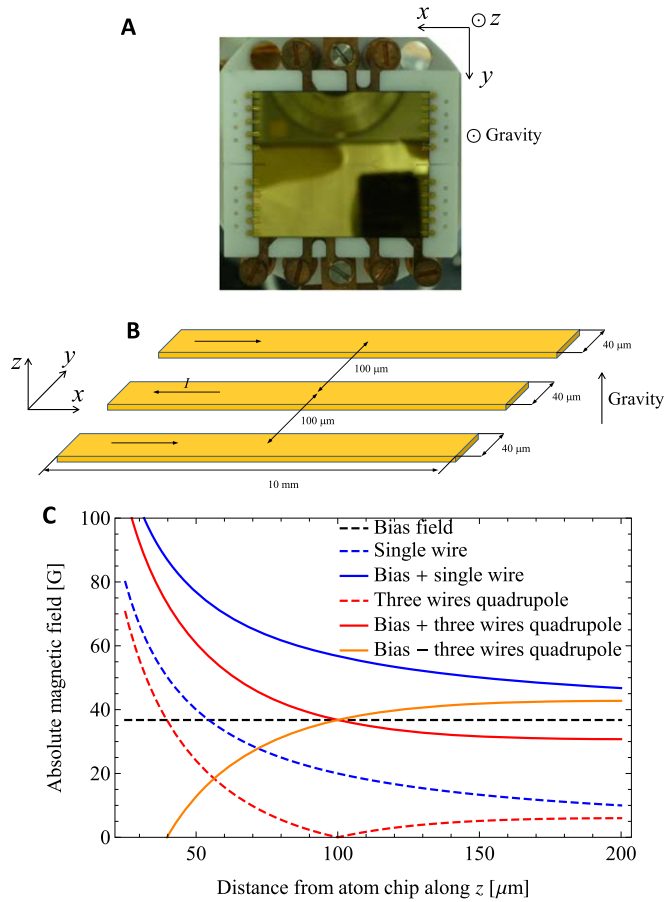


Figure 7. Quadrupole field generation and its benefit. (A) A picture of the atom chip (golden surface) on its mount, where copper wires used for generating the BEC are visible behind it. Note that its orientation in the experimental setup is face down. (B) Schematic diagram of the chip wires which are used to generate the quadrupole field. Wires are 10 mm long, 40 μm wide and 2 μm thick. The separation of the wires' centers is 100 μm, and the direction of the current I alternates from one wire to the next. The wires, being much smaller than the chip, are hardly visible in (A). (C) The constant bias magnetic field (dashed black line) is necessary in order to create a robust quantization axis for the experiment as well as an effective two-level system by inducing a nonlinear Zeeman shift. The bias field is produced by external coils while the chip wires produce the gradients giving rise to the magnetic force. One can see that the total magnitude of the magnetic field produced by a quadrupole and a bias (red line) is smaller than that produced by a single wire and a bias (blue line, as used in [20]), while the gradient (at ~ 100 μm) is the same. Since the phase noise is largely proportional to the magnitude of the magnetic field created during the splitting pulse [20], positioning the atoms near the quadrupole center (98 μm below the chip surface) reduces the phase noise. We also show how an opposite gradient is produced by an opposite current in the three chip wires.

dependence of the normalized multi-shot visibility on the initial wave-packet position when the other parameters are kept constant. Ideally the visibility would be maximal when the atoms are closest to the quadrupole center at $z = 98$ μm, namely, when we release the atoms from the trap at $z_{\text{trap}} = 94$ μm (taking into account a 4 μm falling distance before we apply the splitting pulse). However, the initial position of the atoms also affects the magnitude of the magnetic field gradient (related to the amount of momentum $\hbar k$ imprinted on the cloud) and the field's curvature. This influences the stability of later stages of the interferometric process, such as relative stopping of the two wave packets by the second gradient pulse, so that the maximal visibility may require some adjustment relative to the above points. In this work we did not perform a full combined optimization of the initial trapping position and the delay and stopping pulse durations, but rather used a constant trapping position of about $z_{\text{trap}} = 87.5$ μm and optimized the duration of the delay and stopping pulses, as described in the following.

Above, we discussed the optimal atom position at the start of the interferometer. An important effect we need to consider next are shot-to-shot fluctuations in the latter position. These fluctuations are induced by uncertainties in the position of the magnetic trap in which the BEC is formed. We note that if the stopping parameters are optimized, we expect the initial position fluctuations of the atoms to play a very minor role in the final multi-shot visibility. As shown in section 4, if the stopping pulse is designed to almost completely stop the relative motion of the centers of the two wave packets, then the final shape of the fringe pattern, including its final position, is the same as the shape of the fringe pattern formed just after the splitting pulse, up to a scaling factor. As the phase of the fringes after the splitting pulse, namely the position of their peaks, are determined only by the magnetic field gradient and not by the envelope of the initial wave packet, shifts in

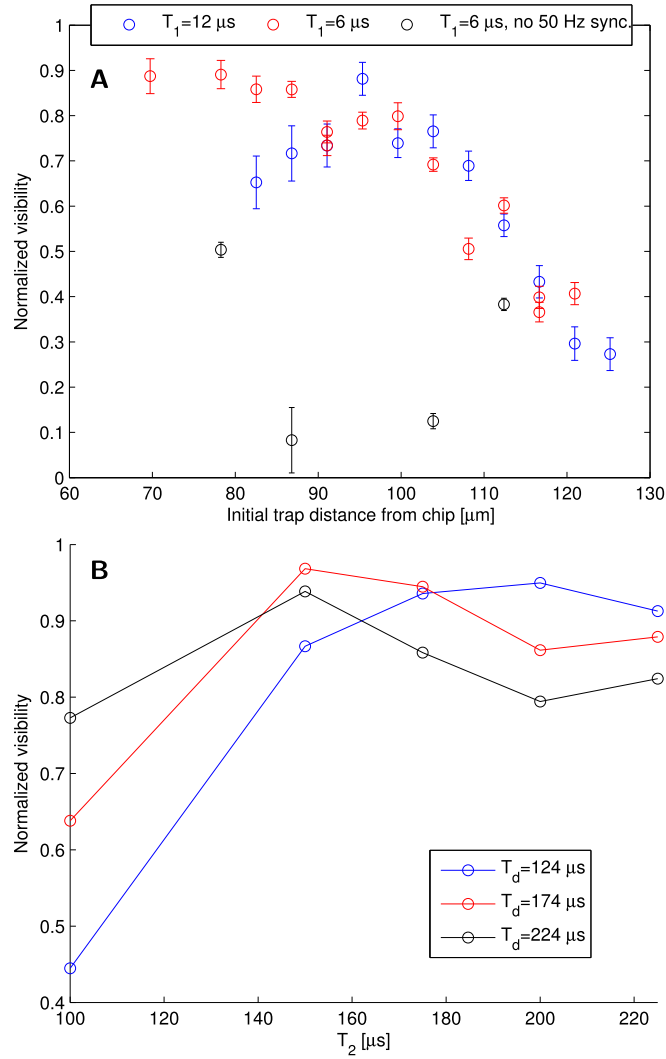


Figure 8. Optimization: (A) normalized multi-shot visibility as a function of the initial trap distance from the atom chip. The other experimental parameters are $(T_1, T_d, T_2) = (6, 104, 130) \mu\text{s}$ and $(12, 158, 180) \mu\text{s}$. Minimal visibility reduction due to magnetic fluctuations during splitting is expected when the splitting position ($4 \mu\text{m}$ farther than the trapping distance due to free fall between trap release and gradient time) is closest to the quadrupole center (at $z = 98 \mu\text{m}$). In practice the visibility may also be governed by imperfections in the later stages of the sequence if the parameters are not optimized for each measurement point. The low visibility data in this plot shows the consequence of lack of synchronization with the 50 Hz electricity grid. (B) Normalized multi-shot visibility as a function of the stopping gradient pulse duration T_2 for a given splitting pulse duration ($T_1 = 6 \mu\text{s}$) and a few values of free propagation time between the gradient pulses, T_d . We expect maximal visibility when the stopping pulse is designed to most accurately stop the relative wave packet motion ($T_2 = \text{acot}(\omega T_d)/\omega$, see equation (9)). Corresponding nominal optimal values for $T_d = 124, 174$ and $224 \mu\text{s}$ are $T_2 = 202, 170$ and $144 \mu\text{s}$, respectively, for an estimated curvature of $\omega = 2\pi \times 800 \text{ Hz}$.

the initial position of the wave packets before the splitting kick will not cause any phase shifts. It follows that the positions (phase) of the observed fringes are expected to be independent of the initial wave-packet position, even if the envelopes of the fringe patterns move, as was reported in previous work [20].

Following the above understanding, in figure 8(b) we optimize the stopping of the relative wave-packets' motion after the free propagation time T_d . For a fixed initial trapping position (which is relatively close to the quadrupole center) we change the second gradient pulse time T_2 for several propagation times T_d . For each value of the propagation time T_d , maximal normalized multi-shot visibility is observed at a corresponding stopping time T_2 for which we believe that a full stopping of the relative wave-packet motion is achieved.

Next, to suppress noise from the 50 Hz electrical grid noise which is coupled to the atoms through the bias coils' current supplies, we synchronize the experimental cycle start time to the phase of the electrical grid sine wave (this is done by using a phase-lock loop, which sends a trigger to the experimental control). In our experiment this significantly reduced this type of noise (see figure 8(a)). We further suppress this noise source by minimizing the time in which the wave packets have a different spin to $40 \mu\text{s}$. We have found that the multi-shot visibility is not significantly sensitive to this time interval as long as it is below $200 \mu\text{s}$. As the achieved high normalized multi-shot visibility corresponds to phase fluctuations of less than 0.5 rad for this time period, we

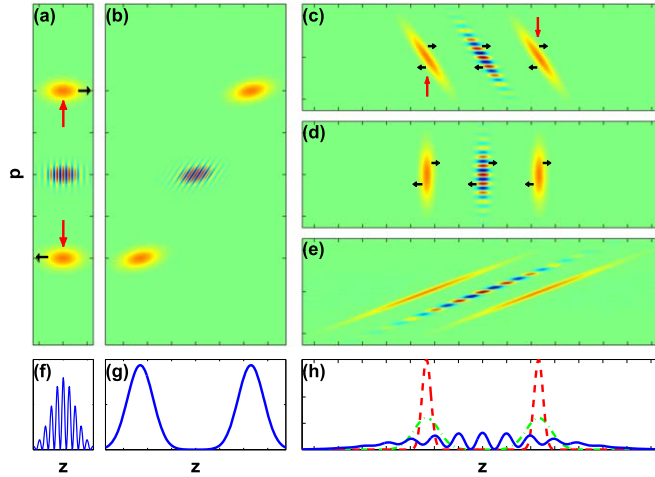


Figure 9. Interferometric sequence in phase space (Wigner function representation, (a)–(e)) and in real space (f)–(h). Positive values of the Wigner function are represented by red and negative values by blue. The initial single wave packet (centered at $p = 0$ and $z = 0$, not shown) is split into two momentum components (a), giving rise to a spatial interference fringe pattern (upon projection onto the position axis, shown in (f)). Red arrows correspond to actions driven by the magnetic field giving rise to the observed wave packet position, whereas black arrows correspond to evolution due to free propagation which follows the present wave packet position in the plot and giving rise to the next plot. (b) and (g): After some free propagation, the wave packets separate. A quadratic potential centered at the middle between the two wave packets performs a phase-space rotation and stops their relative motion ((c) and dashed-dotted green curve in (h)). After some free propagation the phase-space distribution of each wave packet becomes aligned with the momentum axis (d) and the wave-packet size in real space is minimized (dashed red curve in (h)). After a long propagation time an interference fringe pattern is formed ((e) and solid blue curve in (h)), which is a scaled picture of the initial fringe pattern shown in (a) and (f).

can evaluate an upper limit for the fluctuations of the homogeneous bias field B_0 during this time period. For the used value of $B_0 = 36.7$ G, the total accumulated phase difference between states $|1\rangle$ and $|2\rangle$ is $\phi = \mu_B B_0 T / (2\hbar) = 3.2 \times 10^4$ rad. We thus obtain relative fluctuations of $\delta B / B = \delta \phi / \phi \simeq 10^{-5}$.

Additional sources of phase noise are phase measurement uncertainty (due to the fitting procedure) of about 0.1 rad, and chip-to-camera relative position fluctuations (along the direction of the fringes). For the latter, assuming a shot-to-shot instability of 1 and a $31.4 \mu\text{m}$ interference pattern periodicity, these vibrations would create a $2\pi/31.4 = 0.2$ rad phase instability.

Finally, let us note that while each data point in figure 3 is a result of continuous data taking in long sessions ranging in duration from an hour to several hours with no post-selection or post-correction, long term drifts of magnetic fields or voltages in the system (e.g. due to warming up of the copper structure under the chip, the coils or the electronics) were addressed by stopping the data taking and re-optimizing the interferometer. These drifts are not taken into account in the error bars presented in figure 3.

4. Interferometric sequence in phase space

In order to gain a qualitative and quantitative understanding of the interferometric sequence in our experiment, we use the position-momentum phase-space description in the Wigner representation. This description is completely equivalent to the Schrödinger picture in the case where the initial state is a single-particle pure state and allows a generalization to the case of an initial mixed state (e.g. a thermal distribution). This enables us to derive some quantitative analytical estimations of the wave-packet width and separation during certain parts of the sequence, as we show below. Our phase-space description of the atomic dynamics is motivated by our previous work [31], where it was used to analyze the dynamics of an atomic cloud in an anharmonic trap. Our treatment is different from a recent theoretical treatment of the SG experiment with phase-space methods [32], in that we use a scalar distribution function to describe the atoms at the time where the two wave packets have the same internal state.

The phase-space dynamics in the SG spatial fringe interferometer are demonstrated in figure 9. The wave function is manipulated to be a superposition of two wave packets with the same spin just after the splitting stage, such that the scalar Wigner function representation is appropriate. If the gradient pulses are fairly well approximated by a linear+quadratic potential then phase space dynamics is described by the following Newton's equations of motion

$$\frac{d}{dt} \begin{pmatrix} z \\ p \end{pmatrix} = \begin{pmatrix} p/m \\ -m\omega^2 z + F \end{pmatrix}, \quad (5)$$

where F is a homogeneous force (due to a magnetic gradient or gravity) and ω is a harmonic frequency determined by the curvature of the potential. The solution of such a dynamics for all phase-space points z and p is obtained by separating the dynamics into the center-of-mass motion governed by the homogeneous force F and the motion relative to the center of mass, which is governed by the harmonic force. In what follows we concentrate on the second part of the dynamics—relative to the center of mass—which determines the relative position and momentum of the two wave packets and the shape of each of them (expansion or focusing). From here on the phase space variables z and p will therefore denote the position and momentum relative to the center of mass of the two wave packets and in this frame of reference we assume $F = 0$. During a single interferometer stage with a time duration t we will assume for simplicity that the harmonic frequency ω is constant, so that phase space transformation from time t_0 to $t_0 + t$ is described by a rotation $\begin{pmatrix} z(t_0 + t) \\ p(t_0 + t) \end{pmatrix} = \mathcal{R}(\omega, t) \begin{pmatrix} z(t_0) \\ p(t_0) \end{pmatrix}$, where the rotation matrix is

$$\mathcal{R}(\omega, t) = \begin{pmatrix} \cos \omega t & \frac{\sin \omega t}{m\omega} \\ -m\omega \sin \omega t & \cos \omega t \end{pmatrix}. \quad (6)$$

In the limit $\omega \rightarrow 0$ the rotation in equation (6) describes free space propagation

$$\mathcal{R}(0, t) \equiv \lim_{\omega \rightarrow 0} \mathcal{R}(\omega, t) = \begin{pmatrix} 1 & t/m \\ 0 & 1 \end{pmatrix}. \quad (7)$$

After a short splitting pulse of duration T_1 , inducing a momentum difference $\hbar k$ between the two wave packets, they are centered, in the center-of-mass frame, at momenta $p = \pm \hbar k/2$, while the effects of the splitting pulse on the wave-packet shapes are neglected (since $\omega T_1 \ll 1$). During this momentum kick the two wave-packet centers move to a distance $\pm \hbar k T_1 / 4m$ from the origin of the center-of-mass frame. We set the time to be $t = 0$ at the middle of the splitting pulse, such that the center positions $Z = \pm \hbar k t / 2m$ and center momenta $P = \pm \hbar k / 2$ at the end of the pulse ($t = T_1/2$) are the same as if the two wave packets freely propagated from $Z = 0$ at $t = 0$ with the same momenta (capital Z and P representing wave-packet centers). This will be the starting point of our scheme (figure 9(a)).

After a time T_d of free propagation (free fall) the spatial distance between the wave packets is $\hbar k (T_1/2 + T_d) / m$ (figure 9(b)). The stopping pulse of duration T_2 is represented by a harmonic potential of frequency ω that rotates phase space such that the final wave-packet centers lie on the z axis ($P = 0$, figure 9(c)). As we see below, this pulse also serves to focus the wave packets into a minimal wave-packet size. After this pulse the center coordinates become

$$\begin{pmatrix} Z(\tilde{T}_d + T_2) \\ P(\tilde{T}_d + T_2) \end{pmatrix} = \mathcal{R}(\omega, T_2) \mathcal{R}(0, \tilde{T}_d) \begin{pmatrix} 0 \\ \pm \hbar k / 2 \end{pmatrix} = \pm \frac{\hbar k}{2} \begin{pmatrix} \frac{\tilde{T}_d}{m} \cos \omega T_2 + \frac{1}{m\omega} \sin \omega T_2 \\ -\omega \tilde{T}_d \sin \omega T_2 + \cos \omega T_2 \end{pmatrix}, \quad (8)$$

where $\tilde{T}_d \equiv T_d + T_1/2$ is the effective free propagation time. The stopping pulse of length T_2 is designed such that $P(\tilde{T}_d + T_2) = 0$. Under this condition

$$\sin \omega T_2 = \frac{1}{\sqrt{1 + \omega^2 \tilde{T}_d^2}}, \quad \cos \omega T_2 = \frac{\omega \tilde{T}_d}{\sqrt{1 + \omega^2 \tilde{T}_d^2}}. \quad (9)$$

Note that the condition for stopping $\omega \tilde{T}_d \tan \omega T_2 = 1$ does not depend on the splitting momentum kick or the initial center-of-mass position and momentum, so that fluctuations in these parameters are not expected to affect the phase of the final interference fringes as long as the stopping pulse is optimized. However, as we show below, fluctuations of the splitting momentum kick are expected to affect the distance between the wave packets after stopping and consequently the periodicity of the interference fringes measured in the experiment.

We now look at the state of the atoms after another free-propagation time \tilde{T}_d . As shown in figure 9(d), at this time the slanted shape of the phase-space distribution of each of the wave packets aligns with the phase-space coordinates and a minimal wave-packet size in the z direction is achieved, given that the initial wave packets in the middle of the splitting pulse are minimal uncertainty wave packets. To show this, note that the combination of the three operations: propagation for a time \tilde{T}_d , harmonic stopping pulse for a time T_2 satisfying equation (9) and another propagation time \tilde{T}_d transforms general phase-space coordinates as

$$\mathcal{R}(0, \tilde{T}_d) \mathcal{R}(\omega, T_2) \mathcal{R}(0, \tilde{T}_d) \begin{pmatrix} z \\ p \end{pmatrix} = \begin{pmatrix} \frac{\xi}{m\omega} p \\ -\frac{m\omega}{\xi} z \end{pmatrix}. \quad (10)$$

This sequence leads to a complete rotation of phase space by 90° , while scaling the phase-space coordinates by the squeezing factor

$$\xi = \sqrt{1 + \omega^2 \tilde{T}_d^2} = \frac{1}{\sin(\omega T_2)}. \quad (11)$$

At this time the spatial distribution consists of two wave packets at $Z = \pm d/2$, where

$$d = \frac{\xi}{m\omega} \hbar k, \quad (12)$$

and where in the limit of fast stopping relative to the propagation time $\omega \tilde{T}_d \gg 1$ the distance is $d \rightarrow \hbar k \tilde{T}_d / m$.

Subsequent evolution after $t_0 = 2\tilde{T}_d + T_2$ transforms phase-space coordinates as $z \rightarrow z + p\tau/m$, where $\tau = t - t_0$, so that the variance of the spatial distribution of each wave-packet around its center position $Z = \pm d/2$ is

$$\langle \delta z(\tau)^2 \rangle = \left(\frac{\xi}{m\omega} \right)^2 \langle \delta p(0)^2 \rangle + \left(\frac{\omega\tau}{\xi} \right)^2 \langle \delta z(0)^2 \rangle - 2 \frac{\tau}{m} \langle \delta z(0) \delta p(0) \rangle. \quad (13)$$

If at $t = 0$ the two phase-space variables are not correlated ($\langle \delta z(0) \delta p(0) \rangle = 0$) then the wave-packet width has a minimum at $\tau = 0$ ($t = t_0$), where the atomic cloud is focused. More specifically, if the initial wave packet at $t = 0$ is a minimal uncertainty state where the initial position and momentum uncertainties satisfy $\sqrt{\langle \delta z(0)^2 \rangle \langle \delta p(0)^2 \rangle} \equiv \sigma_{z,0} \sigma_{p,0} = \hbar/2$, then the distribution corresponding to each of the two wave packets at time t_0 is focused and has a minimal spatial width

$$\sigma_{\min} = \frac{\xi}{m\omega} \sigma_{p,0} = \frac{\hbar \xi}{2m\omega \sigma_{z,0}}. \quad (14)$$

Note that if the initial momentum kick is large enough to fully separate the two wave packets, namely, $\hbar k \gg \sigma_{p,0}$, then after the full stopping at time $t_0 = 2\tilde{T}_d + T_2$ the distance between the two wave packets is much larger than their size $d/\sigma_{\min} = \hbar k/\sigma_{p,0} \gg 1$, allowing for multiple fringes to be observed.

More generally, correlations between the phase-space variables may exist, for example, when the wave-packet starts to expand over a time T_i before the splitting, as in our experiment, such that $\langle \delta z(0) \delta p(0) \rangle = T_i \sigma_{p,-T_i}^2 / m$. In this case, which may be represented by a slanted phase-space distribution in figure 9(a), minimum cloud size is achieved later at $t = t_0 + \langle \delta z(0) \delta p(0) \rangle \xi^2 / m\omega^2 \langle \delta z(0)^2 \rangle$. The minimum cloud size is then given by

$$\sigma_{\min} = \frac{\xi}{m\omega} \sqrt{\langle \delta p(0)^2 \rangle - \frac{\langle \delta p(0) \delta z(0) \rangle^2}{\langle \delta z(0)^2 \rangle}} \rightarrow \frac{\xi}{m\omega} \sigma_{p,-T_i} \frac{\sigma_{z,-T_i}}{\sqrt{\sigma_{z,-T_i}^2 + (\sigma_{p,-T_i} T_i / m)^2}}, \quad (15)$$

where the right term is for an uncorrelated distribution at $t = -T_i$.

After stopping the relative motion between the two wave packets they are allowed to expand in free space for a long time T_F until they overlap and form a spatial interference pattern at a large scale (figure 9(e)), which is equivalent to applying $\mathcal{R}(0, T_F - \tilde{T}_d)$ for $T_F \gg md/\hbar\sigma_{p,f}$, where $\sigma_{p,f} = m\omega\sigma_{z,0}/\xi$ is the final momentum width. We obtain a spatial fringe pattern with fringe periodicity

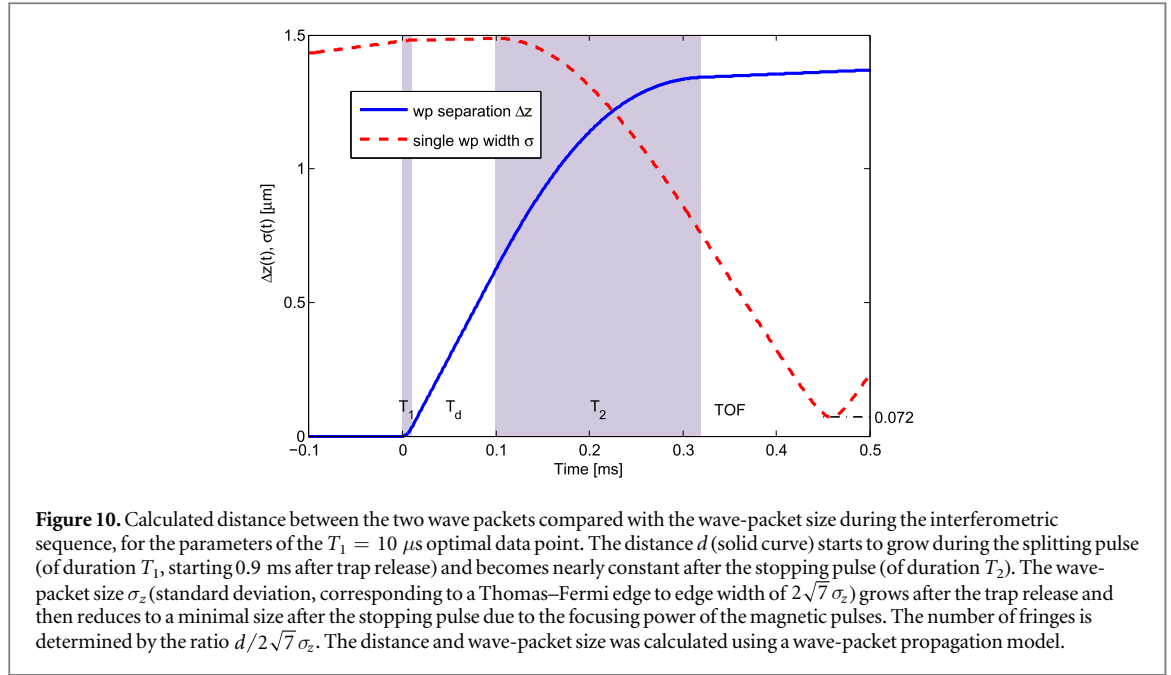
$$\lambda = \frac{2\pi \hbar t}{md} = \frac{2\pi \omega T_F}{k\xi} \quad (16)$$

and an overall envelope width

$$\sigma_{z,f} = \frac{\sigma_{p,f} T_F}{m} = \frac{\sigma_{z,0} \omega T_F}{\xi}. \quad (17)$$

From equations (16) and (17) it follows that the periodicity and envelope size of the final fringe pattern are those of the microscopic fringe pattern formed during the splitting (having a periodicity $\lambda = 2\pi/k$ and width $\sigma_{z,0}$) multiplied by a scaling factor $\omega T_F/\xi$. The number of observed fringes is also the same in the two patterns $n_{\text{fringes}} \approx 2\sigma_{z,f}/\lambda = k\sigma_{z,0}/\pi$. More generally the total experimental sequence is a rotation of phase space by 180° , such that the final pattern observed in the experiment is the same as the microscopic pattern formed just after splitting but scaled by a factor $\omega T_F/\xi$.

The analytical results of the above phase-space analysis are used (see table 1) to predict some wave-packet parameters for the gradient pulse durations used for the data points in figure 3. For comparison we present in figure 10 numerical results of the wave-packet propagation method (see section 3.3) describing the evolution of the wave packets in our interferometer. The process consists of an initial free-fall of the released atomic cloud for



0.9 ms, then splitting for $T_1 = 10 \mu\text{s}$, free-fall for $T_d = 90 \mu\text{s}$ and a stopping pulse for $T_2 = 220 \mu\text{s}$ (same parameters as for the optimal $T_1 = 10 \mu\text{s}$ data point in figure 3). The differential momentum applied during the splitting is $P/m = 6.23 \text{ mm s}^{-1}$ and the harmonic frequency during the stopping pulse ranges between $\omega = 2\pi \times 950 \text{ Hz}$ and 650 Hz due to the fact that the center-of-mass of the two wave packets is accelerated by the magnetic potential and gravity and reaches a distance of $z \approx 124 \mu\text{m}$ from the chip after the stopping pulse. By taking an average harmonic frequency $\bar{\omega} \approx 2\pi \times 800 \text{ Hz}$ we verify that the stopping pulse duration satisfies the stopping requirement $\bar{\omega}\tilde{T}_d \tan \bar{\omega}T_2 \approx 1$ (where $\tilde{T}_d = T_d + T_1/2 = 95 \mu\text{s}$). The wave-packet width (dashed curve) reaches a minimal size of $\sigma_{\min} = 0.072 \mu\text{m}$, $139 \mu\text{s}$ after the end of the stopping pulse. Note that according to the above phase-space analysis a minimal size of $0.065 \mu\text{m}$ is expected to be achieved $\sim \tilde{T}_d = 95 \mu\text{s}$ after the stopping (taking the initial Gaussian width before expansion to be $1.2 \mu\text{m}$). This gives a fairly good estimation of the minimum wave-packet size, while the discrepancy in the focusing time can be attributed to the mean-field repulsive force of atom-atom interactions, which tend to increase position-momentum correlations during the evolution and is neglected in the phase-space analysis. The distance d between the wave packets (solid line) at the focusing point turns out to be $d = 1.32 \mu\text{m}$, compared to the analytical value $d = 1.37 \mu\text{m}$ (from equation (12)) and the measured value $d = 1.31 \mu\text{m}$ (see table 1, 4th column).

5. Conclusions

To conclude, we have demonstrated a high-stability spatial fringe interferometer based on SG splitting of cold atoms by a magnetic field gradient. The atomic spin is used for controlling the motion of the atoms throughout the interferometric sequence, but while the splitting is based on two spin states, it is followed by a stage where the atoms in the two interferometer arms have the same spin state and the interferometric signal is based only on spatial degrees of freedom. In this way we avoid sensitivity to magnetic noise, which gives rise to classical phase uncertainties, as well as quantum decoherence. The fact that we terminate the spin-path entanglement, also means that we do not need to actively recombine the paths, a procedure very sensitive to experimental imperfections [25], as we can simply get interference by allowing the wave packets to expand until they overlap.

We have analyzed the experimental results of the interferometer using several theoretical models, which show good agreement. These models will be important for future experimental optimization procedures, which can become faster and more efficient. In addition, we presented a simple analytical phase-space description of the interferometer.

Our analysis of the interferometric sequence shows that we have separated the two arms of the interferometer to a distance larger by a factor of 8–33 than the atomic wave-packet width before the wave packets at the two arms are allowed to expand, overlap and form interference fringes. The maximal separation between the interferometer arms in the scheme used in this experiment is not limited by the precision or stability of the interferometer but rather by the restricted time of flight and the resolution of the optical imaging device.

Within the whole range of momentum and distance of separation that was implemented we have demonstrated a multi-shot visibility of more than 90%, corresponding to a phase instability of less than $\delta\phi \sim \sqrt{-\log(0.9)} = 0.32$ radians out of a maximum phase difference between the two arms of about ~ 400 radians for the longest splitting pulse length of $T_1 = 16 \mu\text{s}$. This corresponds to a relative phase uncertainty of $\delta\phi/\phi \lesssim 10^{-3}$. The momentum instability at the end of the sequence is found to be less than $\delta k \sim \sqrt{-\log(0.9)}/\sigma \sim 3.2 \text{ mm}^{-1}$ (using equation (3), where $\sigma \sim 100 \mu\text{m}$ is the width of the multi-shot pattern), which is smaller by about 4 orders of magnitude than the maximum momentum splitting of $k \sim 14.5 \mu\text{m}^{-1}$ for $T_1 = 16 \mu\text{s}$. These phase and momentum uncertainties are of the same order as the measured relative current instability of $\delta I/I \simeq 10^{-3}$ for the magnetic gradient pulses in our experiment.

The spatial fringe SGI is limited in maximal spatial splitting, thus limiting its maximum sensitivity, compared to an SGI in which the signal is spin population fringes. This limitation can be overcome by additional accelerating and stopping stages. On the other hand, as explained, it exhibits a high level of robustness which may enable the development of practical applications.

The work presented in this paper proves beyond doubt that there is no strong inherent limit to the coherence in SG splitting, in contrast to some suggestions [33, 34]. It also laid the groundwork to realize a working full-loop SGI interferometer, as presented recently [25, 26]. The full-loop is analogous to the originally envisioned SGI scheme and directly addresses the notion of precision of the magnetic fields, which is the topic of the Humpty-Dumpty effect [25].

Acknowledgments

We thank Zina Binstock for the electronics and the BGU nano-fabrication facility for providing the high-quality chip. This work is funded in part by the Israel Science Foundation (grant No. 856/18) and the German-Israeli DIP project (Hybrid devices: FO 703/2-1) supported by the DFG. We also acknowledge support from the Israeli Council for Higher Education (Israel).

Appendix. Calculation of multi-shot visibility

A.1. Generalized definition of multi-shot visibility

Figure 3 includes engineered instability data used to examine the effect of instability via the multi-shot visibility. These data were obtained by injecting noise into the current driving the splitting pulse, and varying duration of the splitting gradient pulse.

Varying the current generating the first gradient pulse affects both the phase and the periodicity of the fringes (see equation (16)), causing two kinds of chirping effects on the output multi-shot image. The first is a chirp of the interference periodicity, i.e. the image is composed of multiple periodicities (in contrast to a single-shot image or to a high visibility multi-shot image which has only a single periodicity). The second kind is a spatial chirp of the interference visibility, i.e. the visibility is position-dependent. Because of these effects, the visibility of these engineered instability multi-shot images cannot be extracted simply by fitting the pattern to equation (1) as we do in all other images, and we need to adopt a more general definition of the visibility. Here we explain the procedure of extracting the visibility of these multi-shot images.

Assuming our interference pattern is composed of an envelope (e.g. a Gaussian) multiplied by some oscillating function, one possible definition for the interference visibility is to take the Fourier transform of the interference pattern. In κ -space, the result is a sum of three terms: one centered around $\kappa = 0$ —representing the envelope, and the two others at $\kappa = \pm\kappa_0 = \pm 2\pi/\lambda$ —representing the oscillating terms. The visibility can then be defined as the ratio of amplitudes of the oscillatory components to the amplitude of the zero component: $V \equiv [A(+\kappa_0) + A(-\kappa_0)]/A(0)$, where $A(\kappa)$ represent the amplitudes of the Fourier transform at point κ . The visibility of the output multi-shot images is calculated according to this definition by using a numerical FFT of each multi-shot image.

A.2. Theoretical expression

Here we develop a mathematical relation between the interference visibility (in its generalized definition described above) and different experimental noise sources. These noise sources may be studied by examining the statistics of different features of the single-shot interference fringes, such as the central phase and periodicity and here we wish to understand how this statistics determines one number—the stability criterion in this paper, namely the normalized multi-shot visibility V_{ms} .

The Fourier transform of a single interference pattern of the form of equation (1) $\propto e^{-(z-z_0)^2/2\sigma^2} [1 + V_s \cos(\kappa_0 z + \phi)]$ is

$$A(\kappa) = A_0 e^{-i\kappa z_0} \left[e^{-\sigma^2 \kappa^2 / 2} + \frac{1}{2} V_s e^{i(\phi + \kappa_0 z_0)} e^{-\sigma^2 (\kappa - \kappa_0)^2 / 2} + \frac{1}{2} V_s e^{-i(\phi + \kappa_0 z_0)} e^{-\sigma^2 (\kappa + \kappa_0)^2 / 2} \right]. \quad (\text{A1})$$

Here the ratio between the sum of the two side peaks at $\kappa = \pm \kappa_0$ and the central peak is the single-shot visibility V_s , coinciding with the definition of visibility arising from equation (1). For computing the multi-shot visibility let us consider three kinds of shot-to-shot fluctuations: (a) phase ϕ fluctuations with standard deviation $\delta\phi$, (b) wave-vector κ_0 fluctuations with standard deviation $\delta\kappa$, and (c) envelope center z_0 fluctuations with standard deviation δz . If the fluctuations of these parameters are not correlated then fluctuations of the phase ϕ reduce the amplitude of the two side peaks by

$$V_{\text{ms}}(\delta\phi) = e^{-\delta\phi^2/2}. \quad (\text{A2})$$

This expression can be obtained by convolving equation (A1) with a normal distribution probability density function with width $\delta\phi$. Periodicity fluctuations of the fringes broaden the side peaks of the sum fringes at $\pm \kappa_0$ so that their maximum amplitude is reduced. Periodicity fluctuations also introduce phase fluctuations through the factors $e^{\pm i\kappa_0 z_0}$ in equation (A1), if the envelopes of the single-shot fringes are not centered at a constant reference point that can be defined as $z_0 = 0$ (which is also the reference point for ϕ). We then obtain for the amplitude of the two side peaks (up to a phase factor)

$$e^{-\sigma^2 (\kappa \pm \kappa_0)^2 / 2} \rightarrow \eta e^{-\frac{1}{2} \eta^2 [\sigma^2 (\kappa \pm \kappa_0)^2 + \delta\kappa^2 z_0^2]}, \quad (\text{A3})$$

where

$$\frac{1}{\eta} \equiv \sqrt{1 + \sigma^2 \delta\kappa^2} \quad (\text{A4})$$

is the broadening factor of the side peaks.

Fluctuations of the central position z_0 affect the shape of the three peaks at $\kappa = 0, \pm \kappa_0$ in the same way and do not affect the visibility (relative amplitudes) by themselves. However, as the position of the center of the pattern appears in the expression in equation (A3) for the reduction of visibility due to periodicity fluctuations, there may be a combined effect of those two kinds of fluctuations. Here we assume that these two fluctuation sources are not correlated and average over z_0 with the mean of z_0 being $\langle z_0 \rangle = 0$, corresponding to a choice of the fringe pattern center as the reference point for the definition of the phase, we obtain $\langle e^{-(i\kappa \pm \kappa_0)z_0 - \eta^2 \delta\kappa^2 z_0^2 / 2} \rangle_{\kappa = \pm \kappa_0} = 1 / \sqrt{1 + \delta z^2 \delta\kappa^2 \eta^2}$. From equation (A3) we can obtain for the visibility due to wave-vector fluctuations

$$V_{\text{ms}}(\delta\kappa) = \frac{1}{\sqrt{1 + \sigma_{\text{ms}}^2 \delta\kappa^2}}, \quad \sigma_{\text{ms}} = \sqrt{\sigma^2 + \delta z^2}, \quad (\text{A5})$$

where σ_{ms} coincides with the envelope size of the multi-shot pattern.

If the fluctuations of the fringe periodicity and phase are due to a common source, such as current fluctuations of the splitting pulse in our experiment, then the phase fluctuations and periodicity fluctuations should be regarded as correlated. We then assume that the phase fluctuations are proportional to the momentum fluctuations as $\delta\phi = z_i \delta\kappa$, where the proportionality factor z_i in the case of the fringes formed just after the splitting pulse in our experiment is the distance of the atoms from the quadrupole center (but it z_i can be another number in different situations). Then the normalized multi-shot visibility for the combined fluctuations becomes

$$V_{\text{ms}} = \frac{1}{\sqrt{1 + \sigma_{\text{ms}}^2 \delta\kappa^2}} \exp \left[-\frac{1}{2} \frac{\delta\phi^2}{1 + \sigma_{\text{ms}}^2 \delta\kappa^2} \right]. \quad (\text{A6})$$

Note that when the wave-vector fluctuations are small such that $\delta\kappa\sigma \ll 1$ and when the reference position for the phase measurement is chosen to be the center of the fringe pattern (i.e. $z_0 = 0$) then both the expression for correlated fluctuations in equation (A6) and the uncorrelated parameters (combination of equations (A2) and (A5)) converge into the same result

$$V_{\text{ms}} \approx \frac{e^{-\delta\phi^2/2}}{\sqrt{1 + \sigma_{\text{ms}}^2 \delta\kappa^2}} \approx e^{-\frac{1}{2}(\delta\phi^2 + \sigma_{\text{ms}}^2 \delta\kappa^2)}. \quad (\text{A7})$$

Note also that the size of the envelope σ used above refers to the size of the single-shot cloud, while σ_{ms} coincides with the envelope size of the multi-shot pattern. However, for the engineered instability data, where the main source of fluctuations is the splitting pulse, our phase-space model teaches us that the final fringe pattern appearing in the measurement are a scaled picture of the atom number distribution just after the splitting pulse. In that case we can interpret σ as the initial BEC cloud size during splitting, while the multi-shot cloud size σ_{ms} may refer to $\sqrt{\sigma^2 + \delta z^2}$, where δz are the fluctuations of the initial BEC cloud position

($\delta z \approx 1 \mu\text{m}$). This interpretation provides similar results as the one taking the measured wave-vector fluctuations and cloud sizes as a basis for the calculation of the visibility.

If the fluctuations in phase, periodicity and center position are all correlated then we obtain

$$V_{\text{ms}} = \frac{1}{[(1 + \sigma^2 \delta \kappa^2)^2 + 4 \delta \kappa^2 \delta z^2]^{1/4}} \times \exp \left[-\frac{1}{2} \frac{\delta \phi^2}{1 + \sigma^2 \delta \kappa^2 + \frac{4 \delta \kappa^2 \delta z^2}{1 + \sigma^2 \delta \kappa^2}} \right]. \quad (\text{A8})$$

Such correlations do appear in our experiment due to the nonlinearity of the splitting and stopping gradient pulses. An atomic wave-packet that is closer to the chip is subject to a larger force that pushes it further away from the chip more than what we would expect if the gradient was linear, so that atoms that are initially trapped closer to the chip get a larger momentum splitting and appear further away from the chip at the time of observation. However, the apparent visibility of the fringes, when measured by fitting its shape to equation (1), is larger than that predicted by the generalized definition of the visibility by a Fourier transform, due to the fact that wave-packets with different periodicities and phases are not fully overlapping in space, such that destructive interference between them is not complete. We would then expect the apparent visibility to be even higher than that calculated above for the case where the center position fluctuations are not correlated with the phase and periodicity fluctuations.

A.3. Standard error of multi-shot visibility

Let us now consider the standard error $\delta V_{\text{ms}}(N)$ of the multi-shot visibility $V_{\text{ms}}(N)$ due to the finite number N in a sample. For simplicity we consider only global phase fluctuations, such that the multi-shot visibility is

$$V_{\text{ms}}(N) = \frac{1}{N} \left| \sum_{j=1}^N e^{i\phi_j} \right| \equiv \frac{1}{N} |S_N|. \quad (\text{A9})$$

We have $V_{\text{ms}}(N)^2 = N^{-2} [(\text{Re } S_N)^2 + (\text{Im } S_N)^2]$, which has the explicit form

$$\frac{1}{N^2} [\text{Re } S_N]^2 = \frac{1}{4N^2} \sum_{j,k} [e^{i(\phi_j + \phi_k)} + e^{i(\phi_j - \phi_k)} + \text{c.c.}], \quad (\text{A10})$$

$$\frac{1}{N^2} [\text{Im } S_N]^2 = \frac{1}{4N^2} \sum_{j,k} [-e^{i(\phi_j + \phi_k)} + e^{i(\phi_j - \phi_k)} + \text{c.c.}]. \quad (\text{A11})$$

By summing over the real part and imaginary part and separating the sum $\sum_j e^{i(\phi_j - \phi_k)}$ into the case $j = k$ and $j \neq k$ we obtain

$$V_{\text{ms}}^2 = \frac{1}{N} \left[1 + \frac{1}{2N} \sum_{j \neq k} (e^{i(\phi_j - \phi_k)} + \text{c.c.}) \right]. \quad (\text{A12})$$

By taking an average over ensembles with Gaussian distribution of the phases and using the identity $\langle e^{i\phi} \rangle = e^{-\langle \phi^2 \rangle / 2}$, the average over each of the $N(N - 1)$ terms in the sum over $j \neq k$ becomes $e^{-\langle \delta \phi^2 \rangle} = \langle V_{\text{ms}} \rangle^2$ and we have

$$\langle V_{\text{ms}}(N)^2 \rangle - \langle V_{\text{ms}}(N) \rangle^2 = \frac{1}{N} (1 - \langle V_{\text{ms}}(N) \rangle^2). \quad (\text{A13})$$

When the distribution of phases is narrow and $\langle V_{\text{ms}} \rangle \sim 1$ the standard error of the multi-shot visibility is small, but when the visibility is small the standard error goes to the limit $\delta V_{\text{ms}} \sim 1/\sqrt{N}$.

ORCID iDs

Yair Margalit  <https://orcid.org/0000-0002-9180-3700>

References

- [1] Gerlach W and Stern O 1922 Der experimentelle Nachweis der Richtungsquantelung im Magnetfeld *Z. Phys.* **9** 349
- [2] Scully M O, Lamb W E Jr and Barut A 1987 On the theory of the Stern–Gerlach apparatus *Found. Phys.* **17** 575
- [3] Wigner E P 1963 The problem of measurement *Am. J. Phys.* **31** 6
- [4] Briegel H J, Englert B-G, Scully M O and Walther H 1997 *Atom Interferometry* ed P R Berman (New York: Academic) p 240
- [5] Englert B-G, Schwinger J and Scully M O 1988 Is spin coherence like Humpty-Dumpty? I. Simplified treatment *Found. Phys.* **18** 1045
- [6] Schwinger J, Scully M O and Englert B-G 1988 Is spin coherence like Humpty-Dumpty? II. General theory *Z. Phys. D* **10** 135
- [7] Scully M O, Englert B-G and Schwinger J 1989 Spin coherence and Humpty-Dumpty: III. The effects of observation *Phys. Rev. A* **40** 1775
- [8] Robert J, Miniatura C, Le Boiteux S, Reinhardt J, Bocvarski V and Baudon J 1991 Atomic interferometry with metastable hydrogen atoms *Europhys. Lett.* **16** 29

- [9] Robert J *et al* 1991 *10th Int. Conf. on Laser Spectroscopy (Font-Romeu, France)* ed M Ducloy *et al* (Singapore: World Scientific) p 258
- [10] Miniatura C, Perales F, Vassilev G, Reinhardt J, Robert J and Baudon J 1991 A longitudinal Stern–Gerlach interferometer: the ‘beaded’ atom *J. Phys. II* **1** 425
- [11] Miniatura C, Robert J, Le Boiteux S, Reinhardt J and Baudon J 1992 A longitudinal Stern–Gerlach atomic interferometer *Appl. Phys. B* **54** 347
- [12] Robert J, Miniatura C, Gorceix O, Le Boiteux S, Lorent V, Reinhardt J and Baudon J 1992 Atomic quantum phase studies with a longitudinal Stern–Gerlach interferometer *J. Phys. II* **11** 601
- [13] Miniatura C, Robert J, Gorceix O, Lorent V, Le Boiteux S, Reinhardt J and Baudon J 1992 Atomic interferences and the topological phase *Phys. Rev. Lett.* **69** 261
- [14] Nic Chormaic S, Wiedemann V, Miniatura C, Robert J, Le Boiteux S, Lorent V, Gorceix O, Feron S, Reinhardt J and Baudon J 1993 Longitudinal Stern–Gerlach atomic interferometry using velocity selected atomic beams *J. Phys. B: At. Mol. Opt. Phys.* **26** 1271
- [15] Baudon J, Mathevet R and Robert J 1999 Atomic interferometry *J. Phys. B: At. Mol. Opt. Phys.* **32** R173
- [16] Boustimi M, Bocvarski V, Brodsky K, Perales F, Baudon J and Robert J 2000 Atomic interference patterns in the transverse plane *Phys. Rev. A* **61** 033602
- [17] Maréchal E, Long R, Miossec T, Bossennec J L, Barbé R, Keller J C and Gorceix O 2000 Atomic spatial coherence monitoring and engineering with magnetic fields *Phys. Rev. A* **62** 53603
- [18] de Leseagno B V *et al* 2003 Stern–Gerlach interferometry with metastable argon atoms: an immaterial mask modulating the profile of a supersonic beam *Eur. Phys. J. D* **23** 25
- [19] Rubin K *et al* 2004 Atom interferometer using two Stern–Gerlach magnets *Laser Phys. Lett.* **1** 184
- [20] Machluf S, Japha Y and Folman R 2013 Coherent Stern–Gerlach momentum splitting on an atom chip *Nat. Commun.* **4** 2424
- [21] Müntinga H *et al* 2012 Interferometry with Bose–Einstein condensates in microgravity *Phys. Rev. Lett.* **110** 093602
- [22] Keil M, Amit O, Zhou S, Groswasser D, Japha Y and Folman R 2016 Fifteen years of cold matter on the atom chip: promise, realizations, and prospects *J. Mod. Opt.* **63** 1840
- [23] Margalit Y, Zhou Z, Machluf S, Rohrllich D, Japha Y and Folman R 2015 A self-interfering clock as a ‘which path’ witness *Science* **349** 1205
- [24] Zhou Z, Margalit Y, Rohrllich D, Japha Y and Folman R 2018 Quantum complementarity of clocks in the context of general relativity *Class. Quantum Grav.* **18** 185003
- [25] Margalit Y, Zhou Z, Dobkowski O, Amit O, Japha Y, Rohrllich D, Moukouri S and Folman R 2018 Realization of a complete Stern–Gerlach interferometer arXiv:1801.02708
- [26] Amit O *et al* 2019 T3-Stern–Gerlach matter-wave interferometer submitted
- [27] Japha Y 2019 A general wave-packet evolution method for studying coherence of matter-wave interferometers arXiv:1902.07759
- [28] Castin Y and Dum R 1996 Bose–Einstein condensates in time dependent traps *Phys. Rev. Lett.* **77** 5315
- [29] Jamison A O, Kutz J N and Gupta S 2011 Atomic interactions in precision interferometry using Bose–Einstein condensates *Phys. Rev. A* **84** 043643
- [30] Meister M, Arnold S, Moll D, Eckart M, Kajari E, Efremov M A, Walser R and Schleich W P 2017 Efficient description of Bose–Einstein condensates in time-dependent rotating traps *Adv. At. Mol. Opt. Phys.* **66** 375
- [31] Zhou S, Chabé J, Salem R, David T, Groswasser D, Keil M, Japha Y and Folman R 2014 Phase space tomography of cold-atom dynamics in a weakly corrugated potential *Phys. Rev. A* **90** 033620
- [32] Gomis P and Pérez A 2016 Decoherence effects in the Stern–Gerlach experiment using matrix Wigner functions *Phys. Rev. A* **94** 012103
- [33] de Oliveira T R and Caldeira A O 2006 Dissipative Stern–Gerlach recombination experiment *Phys. Rev. A* **73** 042502
- [34] Devereux M 2015 Reduction of the atomic wavefunction in the Stern–Gerlach magnetic field *Can. J. Phys.* **93** 1382